Fine structure of viral dsDNA encapsidation

Shawn Walker
Department of Mathematics, 303 Lockett Hall, Louisiana State University, Baton Rouge, Louisiana 70803, USA

Javier Arsuaga*
Department of Cellular and Molecular Biology, Briggs Hall 09, and Department of Mathematics, MSB 2115, University of California Davis, Davis, California 95616, USA

Lindsey Hiltner†
School of Mathematics, 507 Vincent Hall, University of Minnesota, Minneapolis, Minnesota 55455, USA

M. Carme Calderer‡
School of Mathematics, 507 Vincent Hall, University of Minnesota, Minneapolis, Minnesota 55455, USA

Mariel Vázquez§
Department of Microbiology and Molecular Genetics, Briggs Hall 09, and Department of Mathematics, MSB 2150, University of California Davis, Davis, California 95616, USA

(Received 7 July 2019; accepted 19 December 2019; published 18 February 2020)

Unraveling the mechanisms of packing of DNA inside viral capsids is of fundamental importance to understanding the spread of viruses. It could also help develop new applications to targeted drug delivery devices for a large range of therapies. In this article, we present a robust, predictive mathematical model and its numerical implementation to aid the study and design of bacteriophage viruses for application purposes. Exploiting the analogies between the columnar hexagonal chromonic phases of encapsidated viral DNA and chromonic aggregates formed by plank-shaped molecular compounds, we develop a first-principles effective mechanical model of DNA packing in a viral capsid. The proposed expression of the packing energy, which combines relevant aspects of the liquid crystal theory, is developed from the model of hexagonal columnar phases, together with that describing configurations of polymeric liquid crystals. The method also outlines a parameter selection strategy that uses available data for a collection of viruses, aimed at applications to viral design. The outcome of the work is a mathematical model and its numerical algorithm, based on the method of finite elements, and computer simulations to identify and label the ordered and disordered regions of the capsid and calculate the inner pressure. It also presents the tools for the local reconstruction of the DNA "scaffolding" and the center curve of the filament within the capsid.

DOI: 10.1103/PhysRevE.101.022703

I. INTRODUCTION

The formation of liquid crystal phases in DNA condensates in free solution as well as inside viral capsids led to the *chromonic* denomination of a class of lyotropic liquid crystals that also form toroidal shape aggregates in water. A common denominator between both such systems is that they form hexagonal columnar liquid crystal phases. In this article, we apply models of hexagonal columnar nematic liquid crystals and their numerical algorithms, originally developed for lyotropic liquid crystals, to study the organization of a viral genome in an axisymmetric capsid.

Different from liquid crystals consisting of elongated, rodlike molecules found, for instance, in display devices, chromonic liquid crystals consist of planklike molecules that form liquid crystal phases with varying concentration. At low concentration, the molecules stack to form cylindrical aggregates with randomly oriented axial directions, which tend to align and grow in height as the concentration increases. With even further increase, the cylinders cluster so their center axes align in a hexagonal lattice, forming what is known as the hexagonal columnar liquid crystal phase. That is, a crossection perpendicular to the axial direction of a columnar ensemble reveals an hexagonal lattice, whose vertices are determined by the intersection of the cylinder axes with the plane. On adding concentrating agents such as polyethylene glycol (PEG) and spermedine, the cylinder clusters rearrange into toruslike shapes [1], topologically analogous to those formed by DNA in free solution, also in the presence of condensing agents. DNA aggregates are of the order of magnitude of 10^{-6} of the typical size of a molecular chromonic cluster.

Indeed, experimental and theoretical studies acquired since the late 1980s [2–8] have shown that encapsidated DNA molecules form an hexagonal columnar liquid crystal phase.

*jarsuaga@ucdavis.edu
†hilt010@umn.edu
‡calde014@umn.edu
§mariel@math.ucdavis.edu

 ©2020 American Physical Society

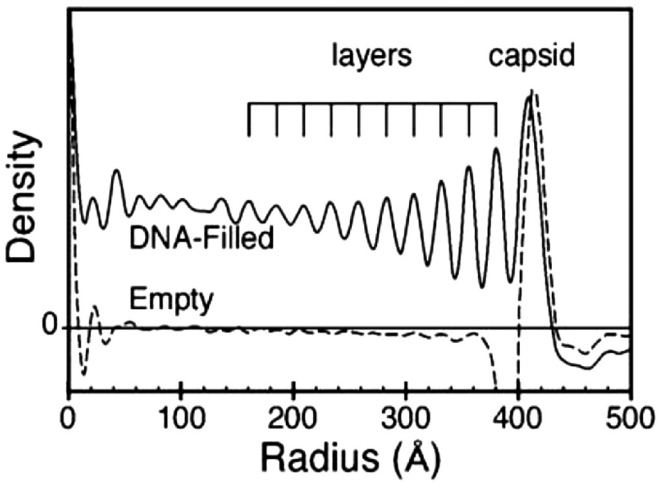

FIG. 1. The graph represents the DNA density of bacteriophage T5. It shows the radial density distribution of DNA inside the viral capsid. The dashed line shows the density of an empty capsid. Figure reproduced from Ref. [16].

In particular, liquid crystalline phases in bacteriophages were first proposed in Ref. [9], with an explicit reference to hexagonal packing made in Ref. [10] and since then consistent data have been accumulating [5,11–14].

This article studies the liquid crystal ordering of viral dsDNA in a capsid with axial symmetry. We combine liquid crystal models and their numerical implementation to determine the equilibrium structure of the DNA in the capsid and the forces that it sustains in the long run. The model is aimed to be used as a tool for the design and prediction of encapsidated DNA in response to the renewed interest in bacteriophages in medicine and biotechnology. This goal guides our parameter selection strategy which is also a main component of the work. The proposed method delivers a parameter phase space for the pressure and the size of the inner disordered core. Moreover, the model and numerical algorithm can integrate additional physics, such as the presence of water, capsid permeability, and the direct effects of ions and DNA charge. This opens the door to a broad range of future studies.

Icosahedral bacteriophages contain a protein capsid whose assembly is followed by the packing, by means of a molecular motor, of a single naked dsDNA molecule [15]. Cryo-electron microscopy (Cryo-EM) images show a well ordered, spool-like, genome arrangement in the outer region, next to the capsid wall, becoming disordered in a central core, a feature shown in a density graph obtained from one of such images (Fig. 1). The DNA molecule inside the viral capsid is found under extreme concentration, between 200 and 800 mg/ml [9], and pressure estimated in the range between 40 and 60 atmospheres (atm) [17,18]. Three factors contribute to the excess pressure found inside the viral capsid: the decrease in entropy associated with the confinement imposed by the capsid, the high resistance of the DNA molecule to bending beyond its persistence length, and the self-repulsion of the DNA molecule [19]. At the time of infection the DNA is released by a mechanism that suggests a phase transition, possibly into a "liquidlike" state [3,20,21]. Both processes, packing and releasing of the genome, depend greatly on how the DNA molecule folds within the viral capsid; however, our understanding of this folding remains very limited.

A first-principles model of DNA encapsidation would consider a very long flexible rod of finite thickness (dsDNA molecules) that resists bending and is packed inside a rigid container (for instance, see Ref. [22]). Difficulties with this approach, in addition to accounting for the electrostatic interactions, would stem from treating constraints to prevent self-overlapping, which would result in a very challenging numerical problem. Indeed, in Ref. [23], the authors used Monte Carlo methods to study DNA packing by a similar "direct" model. Unfortunately, these methods are computationally expensive, which makes exploration of DNA packing in bacteriophages nearly intractable. Likewise, the methods of Brownian dynamics are severely limited by the size of the DNA molecule [24,25].

Therefore, we adopt a phenomenological viewpoint and develop a continuum mechanical model of DNA encapsidation based on the theory of hexagonal columnar liquid crystals, formulated in terms of director fields, together with that of liquid crystals with variable degree of orientation. The latter brings an additional scalar field, the degree of orientation $s \in [0, 1)$, into the model [26]. The value $s = 0$ corresponds to the isotropic state, with random molecular orientation, and the ideal value $s = 1$ representing perfect alignment.

Indeed, one difficulty with director field models of liquid crystals is that the associated energy may become unbounded at defect locations, that is points, lines, or surfaces where the vector field vanishes. The scalar degree of orientation provides a mathematical tool to regularize field singularities, such as those occurring in DNA crossings and near non-smooth locations in the capsid. Its main role in our work is to characterize the disordered core region of the capsid, labeled with small s, close to 0. The region of the capsid with ordered spooled DNA is characterized by values of s near 1. The rigorous justification of the order parameter s is done in terms of the distinguished eigenvalue of the symmetric, traceless, uniaxial second-order tensor Q obtained from the second-order moment of a probability distribution function defined on the unit sphere $\mathcal{S}^2$.

We describe a hexagonal columnar configuration in terms of a triple of orthonormal vector fields, $\{\mathbf{n}, \mathbf{m}, \mathbf{p}\}$ and the scalar order parameter $s \in [0, 1)$. The director $\mathbf{n}$ gives the local direction of the columnar axis and corresponds to the tangent vector to the DNA center curve at a point. The unit vectors $\mathbf{m}$ and $\mathbf{p}$ correspond to lattice vectors of the orthogonal cross sections and represent the directions along which neighboring strands are found in the encapsidated arrangement (Fig. 3).

The energy that we construct combines the extension of the Oseen-Frank energy by Ericksen to account for the variable degree of orientation [26], in addition to the de Gennes energy of columnar hexagonal liquid crystals [27,28], restricted to the case that the material is made of filaments. An additional term penalizes the area of the interface between the ordered and disordered core regions in the capsid. We note that Ericksen's energy can also be viewed as the restriction of the Landau-deGennes energy of biaxial nematic liquid crystals to uniaxial [29]. Other surface energy terms will be used as well on the surface of the capsid to represent the contact with the DNA. Indeed, the role of the boundary proteins in ordering

the DNA in the capsid, although not yet fully understood, has been the subject of many studies [4,30–32]. We note that Ericksen's model was first developed to model polymeric liquid crystals that tend to develop a wealth of defects and texture during processing [33].

Data at our disposal include the genome length L, the volume V, and radius R_c of the capsid and the cryo-EM images of the bacteriophage that through the ensuing DNA density graphs (Fig. 1) give the effective diameter d of the DNA and the size of the disordered core [31,34–36]. Pressure and concentration data of the encapsidated DNA are also available. We take the customary point of view that the DNA molecule is a semiflexible elastic polymer characterized by the persistence length L_p which is about the size of the radius of the capsid. In the calculation of the bending modulus k_3, we also assume that the hydrated DNA fills the entire volume of the capsid [9], justifying our selection of the maximum linear density m_0. This also allows us to simplify the model since the enthropic energy does not seem to play a main role when the whole genome fills the entire capsid.

The repulsive energy between neighboring DNA strands is not explicitly present in the model but is accounted for by the effective role of the parameters of the mechanical energy.

In order to calculate the minimizer of the total energy, we proceed into two stages, first, neglecting the elastic contribution of the cross section to the filaments. We start considering the total energy of encapsidation as consisting of the bending energy of the DNA filament formulated in terms of the director field $\mathbf{n}$, together with a normalized potential $w(s)$ that attains its minimum value at the ordered configuration, labeled as $s = s_a \approx 1$, and the maximum at $s = 0$, reflecting the preference of the DNA to organize inside the capsid (Fig. 2). A penalty is also associated with changes in s resulting in a transition region between the spooledlike state and the disordered inner core. However, under parameter choices that provide good agreement between the values of experimental and the calculated disordered core sizes, we find that the pressure is underpredicted by a factor of 100 with respect to experimentally measured values [2,17,37–39]. This leads us to include an additional term in the energy penalizing distortions of the cross section formulated as quadratic expressions of the gradients of the cross-sectional vectors $\nabla\mathbf{m}$ and $\nabla\mathbf{p}$, stemming from the hexagonal columnar elastic energy. It is the bulk and shear modulus, B and C, present in the transverse elastic energy, that effectively account for the cohesive effects postulated in earlier models of DNA encapsidation [39,40] that, in turn, also effectively account for the electrostatic interactions.

We find that the dimensionless energy restricted to spooling configurations involves three material constants, $\hat{b}$, $\hat{\gamma}_0$, and α, in addition to k_3 that can be directly calculated from DNA data (Table I). The quantities $\tilde{b}$ and $\tilde{\gamma}_0$ are signature parameters in models of phase transitions, and, in our case, quantify the degree of order-disorder of the configuration. That is, $\tilde{\gamma}$ contributes to controlling the size of the disordered core versus that of the spooled DNA region; a regularization parameter, is related to the area of the (ideal) surface separating both such regions. We determine the orders of magnitude of $\hat{b}$ and $\hat{\gamma}_0$ from the size of the disordered core of the T4 virus, as measured by imaging (see references in Table I). Likewise, the parameter α, used in scaling the elastic moduli B and C with respect to k_3, is estimated from experimental pressure values corresponding to the same viruses [2,17,37–39]. The numerical simulations deliver phase spaces for the radius of the inner disordered core and the pressure, in terms of the parameters $\hat{b}$ and $\hat{\gamma}_0$ (Figs. 2–4).

TABLE I. Physical measurements of four different bacteriophages. The symbol L_p denotes the persistence length of a DNA chain of length L, effective diameter d, in a spherelike capsid of radius R_c with a measured radius r_0 of the disordered core. T4 [41,42], T5 [31], T7 [32], and $\epsilon 15$ [36]. The last column gives the pressure on the capsid.

Virus	L_p (nm)	d (nm)	L (nm)	R_c (nm)	r_0/R_c	Pr.(atm)
T4	52.8	2.4	55047.6	40.0	0.5500	28.70
T5	58.38	2.94	39423.8	42.0	0.4286	30.17
T7	52.88	2.6	12932.0	26.05	0.5889	44.02
$\epsilon 15$	53.9	2.55	12846.0	28.37	0.5735	40.41

Earlier mathematical results on Ericksen's model guarantee existence of a global minimizer of the total energy [43]. In addition, numerical methods previously developed by Walker *et al.* [44–46] on such a model extend to the present case and provide a convenient algorithm to predict packing configurations and the pressure values that they sustain. Cryo-EM images for most bacteriophages show multilayered spoolinglike configurations on the outer layers of the packed genome [2,30–32,34–36]. We present numerical simulations of minimizing configurations with spooling geometry.

In Sec. II, we give a brief review of the nematic and chromonic models of liquid crystals to explain and develop the tools for our methods, with a special emphasis on Ericksen's model that includes the variable degree of orientation field.

In Sec. III, we the energy of packing, its scaling properties and the role of the spooling configurations. In Sec. IV, we present our approach for estimating parameters, concluding with numerical simulations that relate remaining phenomenological parameters to the radius of the inner disordered core. Section V deals with the shape optimization method and its application to calculate the pressures near the capsid surface.

This work is motivated by earlier studies of free boundary problems of chromonic liquid crystals and bacteriophages carried out in the Ph.D. dissertation by Lindsey Hiltner [47] and is partially inspired by Refs. [40,48]. The software supporting the numerical simulations of the model is freely available for download [49].

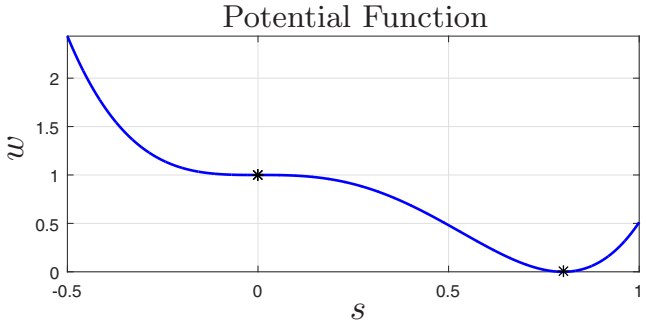

FIG. 2. Plot of the isotropic penalty function w. The asterisks indicate points of zero slope.

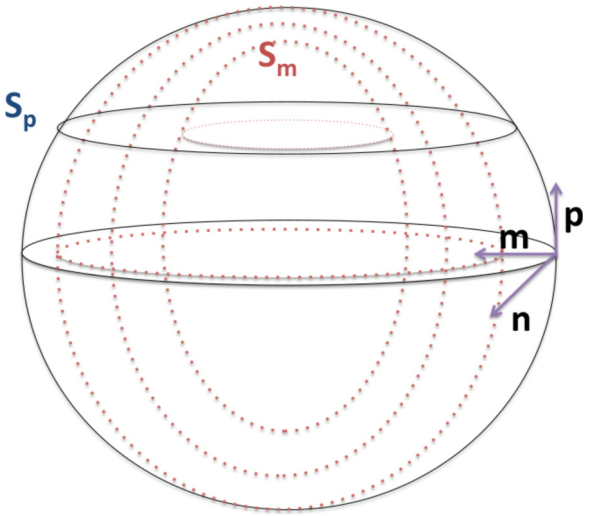

FIG. 3. The graph a schematic representation of the level surfaces $\omega = \text{const}$, $\vartheta = \text{const}$, designated as $\mathcal{S}_m$ and $\mathcal{S}_p$, respectively, whose intersections provide the model scaffolding that supports the DNA filament.

II. NEMATIC AND CHROMONIC LIQUID CRYSTALS

The unit director field $\mathbf{n}$ plays an essential role in the description of order in uniaxial nematic liquid crystals. For rodlike (calamitic) molecules, it represents the average orientation of the long molecular axis and, for planklike molecules (discotic), it corresponds to the average orientation of the normal vector to the disks. Chromonic liquid crystals are of discotic type.

An alternate approach to describing order in liquid crystals is in terms of the symmetric second-order tensor Q. It is the traceless version of a tensor M defined as the second moment of the probability distribution function $\rho(\boldsymbol{x}, \boldsymbol{l}), \boldsymbol{l} \in \mathbb{S}^2$, of the molecular orientation $\boldsymbol{l}$ at a point $\boldsymbol{x}$ of the liquid crystal domain $\Omega \subset \mathbb{R}^3$. That is, $M = \int_{S^2} \rho(\boldsymbol{x}, \boldsymbol{l}) \boldsymbol{l} \otimes \boldsymbol{l}\, d\boldsymbol{l}$ and $Q = M - \frac{1}{3} I$. We recall that the first-order moment of ρ is zero due to the assumption that liquid crystal molecules have indistinguishable ends. In the case that two of the eigenvalues of Q are equal and distinct from the third one, the liquid crystal is optically uniaxial with $Q = s(\mathbf{n} \otimes \mathbf{n} - \frac{1}{3} I)$, $s \in (-\frac{1}{3}, 1)$, and $|\mathbf{n}| = 1$. The eigenvector $\mathbf{n}$ is associated with the optic axis of the material and corresponds to the director field of the Oseen-Frank theory; the scalar s represents the degree of orientation, describing the quality of the molecular alignment with respect to $\mathbf{n}$. The value $s = 1$ corresponds to the ideally perfect alignment and $s = 0$ to the isotropic state, with randomly oriented molecules. In well-aligned nematic liquid crystals, s is found to be in the range 0.5 to 0.9. (The case with $s < 0$ is labeled as negative uniaxiality, with $s = -\frac{1}{2}$ corresponding to the molecules being placed on a plane perpendicular to $\mathbf{n}$.) When the three eigenvalues of Q are distinct, the liquid crystal is biaxial, with two distinguished directions. In the case that the eigenvalues are equal, and equal to 0, $Q = 0$, corresponding to the isotropic state.

A. Nematic liquid crystals

In the Oseen-Frank theory, equilibrium states of a nematic liquid crystal are minimizers of the energy given by

$$E = \int_\Omega \mathcal{W}_1(\mathbf{n}, \nabla \mathbf{n})\, d\boldsymbol{x}, \tag{1}$$

$$\mathcal{W}_1(\mathbf{n}, \nabla \mathbf{n}) = K_1(\operatorname{div} \mathbf{n})^2 + K_2(\mathbf{n} \cdot \operatorname{curl} \mathbf{n})^2 + K_3|\mathbf{n} \times \operatorname{curl} \mathbf{n}|^2 + (K_2 + K_4)[\operatorname{tr}([\nabla \mathbf{n}]^2) - (\operatorname{div} \mathbf{n})^2]. \tag{2}$$

The splay, twist, and bend material constants, $K_1 > 0, K_2 > 0$, and $K_3 > 0$, respectively, are associated with the liquid crystal deformations that embody the corresponding geometries. The splay-bend term multiplying $K_2 + K_4$ is a null Lagrangian and so it depends on boundary values only. Defects in the Oseen-Frank theory correspond to locations, points, lines, or surfaces, where $\mathbf{n} = 0$, that is where the molecular order is lost, giving rise to locally disordered structures that may have infinite energy.

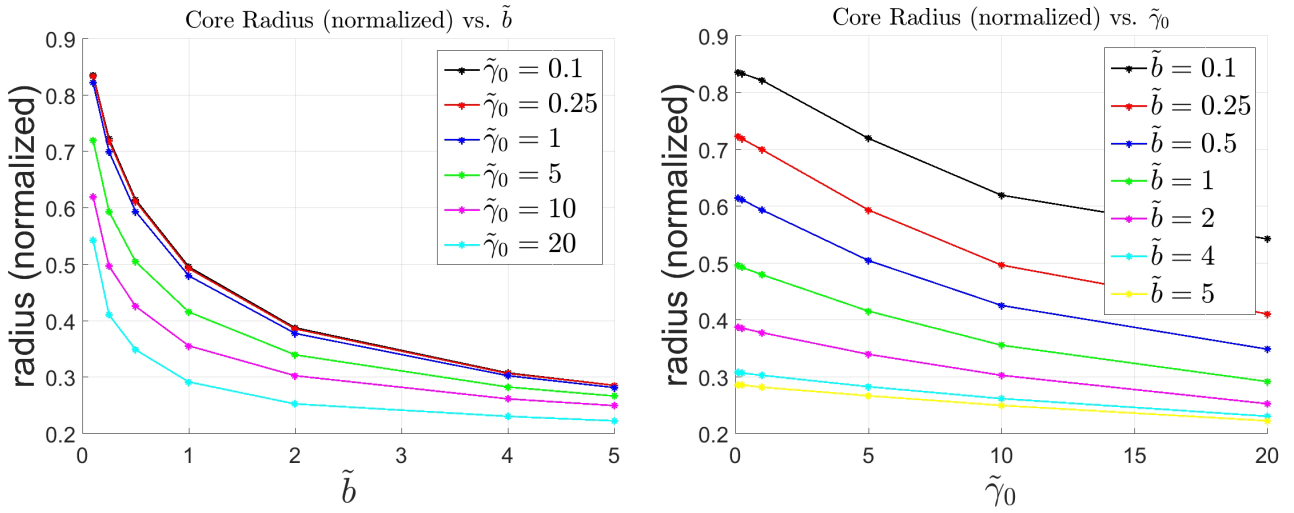

FIG. 4. The graphs show the role of the parameters $\tilde{b}$ and $\tilde{\gamma}_0$ in the model. In both cases, the curves indicate the decrease in core radius with increasing parameter values, as a mechanism to lower the energy of the system. We recall that $\tilde{b}$ represents the surface energy of the transition layer between the spool-like and the disordered regions of the capsid, and $\tilde{\gamma}_0$ corresponds to the bulk energy of the disordered inner core.

In order to represent liquid crystal configurations where ordered and disordered states coexist as well as assign finite energy to defects, we then adopt Ericksen's model [26] of liquid crystals with variable degree of orientation. In this model, the equilibrium state of the liquid crystal material is described by the pair $(s, \mathbf{n})$ minimizing a bulk-energy functional

$$E_{\mathrm{erk}}[s, \mathbf{n}] := \frac{1}{2}\int_\Omega s^2 \mathcal{W}_1(\mathbf{n}, \nabla \mathbf{n}) + b|\nabla s|^2\, d\boldsymbol{x} + \gamma_0 \int_\Omega w(s)\, d\boldsymbol{x}, \tag{3}$$

with $\mathcal{W}_1$ as in Eq. (2). The potential function $w(s)$ is of class C^2, defined on $-1/2 < s < 1$, and penalizes the phase transition between the nematic and the isotropic phases. It is chosen so that it has a minimum at $s = s_a$, s_a being the preferred order parameter value at a given temperature or concentration; it has a local maximum at $s = 0$ indicating the ordering preference of the DNA. We list its properties as follows [26,43,50]:

$$\lim_{s\to 1} w(s) = \lim_{s\to -1/2} w(s) = \infty, \tag{4}$$

$$w(0) = 1,$$

$$w(s_a) = \min_{s\in[-1/2,1]} w(s) = 0, \text{ for some } s_a \in (0, 1), \tag{5}$$

$$w'(0) = 0,\ w \text{ has a local maximum at } s = 0. \tag{6}$$

We will later take $w(s)$ to be quadratic near $s = s_a = 0.8$ (see Fig. 2). From property (5), it follows that the material constant $\gamma_0 > 0$ is a disordered penalty parameter, and $b > 0$ controls the amount of regularization induced by s. In particular, it represents the surface energy of transition between the spool-like and disordered regions of the capsid. A full description of the model can be found in Ref. [26] and its analysis in Refs. [44–46].

Next, we discuss the approach to imposing boundary conditions. Rather than prescribing pointwise values of the fields $(s, \mathbf{n})$ on the boundary, that is, imposing strong anchoring boundary conditions, we appeal to weak anchoring, which consists in penalizing the energy of departure of the boundary values from the ideal ones [51]:

$$\begin{aligned} E_a(s, \mathbf{n}) &:= E_{a,\mathbf{n}}(s, \mathbf{n}) + E_{a,s}(s), \\ E_{a,\mathbf{n}}(s, \mathbf{n}) &:= \frac{1}{2}\int_\Gamma s^2\{a_\perp(\boldsymbol{\nu}\cdot\mathbf{n})^2 + a_\parallel[1 - (\boldsymbol{\nu}\cdot\mathbf{n})^2]\} dS(\boldsymbol{x}), \\ E_{a,s}(s) &:= \frac{1}{2}\int_\Gamma a_{\mathrm{ori}}(s - s_a)^2 dS(\boldsymbol{x}), \end{aligned} \tag{7}$$

where $\boldsymbol{\nu}$ is the oriented unit normal vector of $\Gamma := \partial\Omega$. The first term $a_\perp$ tends to align the minimizing director field $\mathbf{n}$ perpendicular to $\boldsymbol{\nu}$, and the second term $a_\parallel$ favors a parallel alignment. The last contribution to the energy is needed to ensure that s does not trivially vanish on the interface and so cause $E_{a,\mathbf{n}}(s, \mathbf{n})$ to vanish as well [45,52,53]. The parameters $a_\perp, a_\parallel, a_{\mathrm{ori}} : \Gamma \to [0, \infty)$ may vary (in general), but here we take them to be fixed constants.

In determining a configuration of a liquid crystal, one minimizes the total energy consisting of (3) added to (7). A thorough study of existence of minimizers together with the numerical implementation of the minimizing algorithm can be found in Refs. [44–46]. In particular, the theory allows for Ω to be of icosahedral shape, since $s = 0$ at the edges where the vector fields are not defined.

B. Chromonic liquid crystals

We are concerned with hexagonal columnar phases of chromonic liquid crystals. The energy consists of the Oseen-Frank contribution (or the Ericksen's model analog) together with an elastic energy of the cross section perpendicular to the columnar director field $\mathbf{n}$ and spanned by the vectors $\mathbf{m}$ and $\mathbf{p}$; the triple $\{\mathbf{n}, \mathbf{m}, \mathbf{p}\}$ form an orthonormal set (Fig. 3). The energy also effectively includes the electrostatic repulsive energy of the negatively charged DNA strands. We then represent the total energy as

$$E_{\mathrm{chr}} = E_{\mathrm{erk}}[s, \mathbf{n}] + E_{\mathrm{elas}}[\nabla \boldsymbol{u}], \quad \mathbf{n}\cdot\boldsymbol{u} = 0, \tag{8}$$

where $\boldsymbol{u} \in \mathrm{span}\{\mathbf{m}, \mathbf{p}\}$ denotes the displacement vector associated with deformation of the cross section and corresponding energy [27,28]:

$$E_{\mathrm{elas}}[\nabla \boldsymbol{u}] = \tfrac{1}{2}(B|\nabla \boldsymbol{u} + \nabla \boldsymbol{u}^T|^2 + C|\nabla \boldsymbol{u} - \nabla \boldsymbol{u}^T|^2), \tag{9}$$

where $B > 0$ and $C > 0$ denote the bulk and shear modulus of the material, respectively. The minimization of the chromonic energy is done subject to the constraints

$$\mathrm{div}\,\mathbf{n} = 0, \quad \text{and} \quad (\mathrm{curl}\,\mathbf{n})\cdot\mathbf{n} = 0. \tag{10}$$

The splay of a liquid crystal is zero whenever dislocations do not occur, that is, the same number of filaments that enter a unit area exit that cross section. In the case of the hexagonal columnar phase, nonzero splay would allow for deviations from the lattice structure. Twist is prohibited because of its incompatibility with the two-dimensional lattice order in planes perpendicular to the director. However, in our approach, we relax the constraints (10) by taking the corresponding elasticity constants K_1 and K_3, respectively, in the energy as very large.

We observe that the previous model does not reflect the discrete nature of a system made of filament strands. In order to associate a minimizing set $\{\mathbf{n}, \mathbf{m}, \mathbf{p}, s\}$ to a local DNA configuration, given the interstrand DNA spacing taken as its effective diameter, $d > 0$, we further introduce the scalar fields ω, ϑ as solutions of the ordinary differential equations

$$\frac{d\omega}{d\mathbf{m}} = \frac{2\pi}{d}, \quad \frac{d\vartheta}{d\mathbf{p}} = \frac{2\pi}{d}, \quad s \neq 0. \tag{11}$$

Then the intersections of level surfaces $\omega = \mathrm{const}$, $\vartheta = \mathrm{const}$ give the location of the DNA strands, away from points or lines where $s = 0$. Furthermore, the piecewise smooth curve $\boldsymbol{r} = \boldsymbol{r}(\zeta)$, $\zeta \in [0, L]$, such that

$$\frac{d\boldsymbol{r}}{d\zeta} = \mathbf{n}[\boldsymbol{r}(\zeta)], \quad \boldsymbol{r}(0) = \boldsymbol{r}_0, \tag{12}$$

describes the axis of the DNA double helix. Here $L > 0$ represents the length of the genome and $\boldsymbol{r}_0$ its entry point in the capsid.

Representing $\boldsymbol{u}$ in terms of the local coordinates (ϑ, ω) motivates us to postulate the related and simpler elastic energy,

$$E_{\mathrm{elas}}[\nabla \mathbf{m}, \nabla \mathbf{p}] = s^2[B|\nabla(\mathbf{m} + \mathbf{p})|^2 + C|\nabla(\mathbf{m} - \mathbf{p})|^2]. \tag{13}$$

Prior to multiplication by the factor s^2, the previous expression differs from (9) by a constant term and neglects the dependence of the coefficients on (ϑ, ω) keeping, instead, the original elastic moduli.

We conclude this section commenting on the solvability of the ordinary differential equations (11) and (12). As previously noted, they only hold at points of the domain where $s > 0$, that is, where the DNA is well ordered. It follows from results on regularity of minimizers of Ericksen's energy [54,55] that, if $s > 0$ on the boundary of the domain, then $s = 0$ can occur only on sets of Hausdorff measure at most two, that is, surfaces, lines, and points. Furthermore, studies of minimization of the Oseen-Frank energy establish that $\mathbf{n} = 0$ occurs in sets of Hausdorff measure less than 1 [56]. Hence, with no further study, we can only locally reconstruct the DNA strand from its director field $\mathbf{n}$.

III. DNA ENCAPSIDATION

We assume that the capsid and the cavity it encloses corresponds to a bounded, axisymmetric region $\Omega \in \mathbb{R}^3$ with $\partial\Omega$ representing the piecewise smooth, faceted, viral capsid. We let $l_0 > 0$ denote the length of the axis that connects the location of the connector with its antipodal site in the viral capsid. Assuming the DNA is tightly packed inside the capsid, we adopt a continuum approach for representing the configuration of the DNA [40,48]. To this end, we let $\mathbf{n}$ represent the unit tangent vector of an "ensemble" of packed DNA segments. Moreover, we use the s variable (degree of orientation) to represent how well ordered the DNA segments are, e.g., $s = 0$ indicates that the DNA strands are oriented in all directions equally. Furthermore, the unit vectors $\{\boldsymbol{m}, \mathbf{p}\}$ span the cross sections perpendicular to the DNA axis, with its associated level curves representing segment locations.

A. Total energy

The model that we propose consists of the total free energy together with a list of constraints, expressed as follows:

$$E = E_{\text{erk}}[s, \mathbf{n}] + E_a(s, \mathbf{n}) + E_{\text{elas}}[\nabla\mathbf{m}, \nabla\mathbf{p}], \tag{14}$$

$$\mathbf{n}\cdot\mathbf{m} = 0, \quad \mathbf{m}\cdot\mathbf{p} = 0, \quad \mathbf{n}\cdot\mathbf{p} = 0, \tag{15}$$

$$|\mathbf{n}| = |\mathbf{m}| = |\mathbf{p}| = 1. \tag{16}$$

Substitution of expressions (3), (7), and (13) into Eq. (16) gives the total energy of the DNA coiling system:

$$\begin{aligned}\mathcal{E}[s, \mathbf{n}, \mathbf{m}, \mathbf{p}, \Omega] = {} & \frac{1}{2}\int_\Omega s^2(k_1(\operatorname{div}\mathbf{n})^2 + k_2(\mathbf{n}\cdot\operatorname{curl}\mathbf{n})^2 + k_3|\mathbf{n}\times\operatorname{curl}\mathbf{n}|^2 + k_2\{\operatorname{tr}([\nabla\mathbf{n}]^2) - (\operatorname{div}\mathbf{n})^2\})d\boldsymbol{x} \\ & + \frac{1}{2}\int_\Omega b|\nabla s|^2 d\boldsymbol{x} + \gamma_0\int_\Omega w(s)\,d\boldsymbol{x} + \frac{1}{2}a_0\left[\int_\Gamma s^2(\boldsymbol{v}\cdot\mathbf{n})^2 dS(\boldsymbol{x}) + \int_\Gamma (s - s_a)^2 dS(\boldsymbol{x})\right] \\ & + \frac{1}{2}\int_\Omega [Bs^2|\nabla(\mathbf{m} + \mathbf{p})|^2 + Cs^2|\nabla(\mathbf{m} - \mathbf{p})|^2]d\boldsymbol{x}.\end{aligned} \tag{17}$$

We start with the following choices for the parameters of the model:

$$K_1 \approx K_2 \gg K_3, \quad K_4 = 0, \tag{18}$$

$$a_0 := a_\perp = a_{\text{ori}}, \quad a_\parallel = 0, \quad a_0 \approx K_3/R_c, \tag{19}$$

$$b \approx K_3, \quad B \approx K_3 \approx C, \quad A := B + C = \alpha K_3, \tag{20}$$

where $\alpha > 0$ in Eq. (20) is a scaling parameter later determined using pressure measurements. Instead of imposing the constraints (10), the first relation in Eq. (18) reflects the fact that $\operatorname{div}\mathbf{n}$ and $\mathbf{n}\cdot\operatorname{curl}\mathbf{n}$ are almost negligible for the DNA coiling configurations. The selection of the constants (19) in the anchoring energy (7) enforces tangential (planar) boundary conditions for $\mathbf{n}$, as this is consistent with DNA spooling inside capsids. The remaining relations indicate that bending is taken as the reference energy of the model and are statements on the orders of magnitude of the parameters and will be further discussed in a later section. We conclude this section by introducing the additional notation $k_i = K_i + A$, with A as in Eq. (20). In particular, note that

$$k_3 = K_3 + A. \tag{21}$$

B. Spooling configurations

From now on, we consider axisymmetric capsids and spooling configurations. Adopting cylindrical coordinates (r, θ, z), with the z axis along the capsid axis and letting $(\boldsymbol{e}_r, \boldsymbol{e}_\theta, \boldsymbol{e}_z)$ denote the corresponding orthonormal basis, spooling DNA arrangements are characterized by $\mathbf{p} = \boldsymbol{e}_z$. Moreover, for such configurations, it is natural to set $\mathbf{n} = \boldsymbol{e}_\theta$, $\boldsymbol{v} = \boldsymbol{e}_r$ and $s = s_a$ on the boundary. Since $\nabla\mathbf{p} = 0$ and $\mathbf{m} = \mathbf{n}\times\mathbf{p}$, so $|\nabla\mathbf{m}| = |\nabla\mathbf{n}|$. Furthermore, applying the identity

$$(\mathbf{n}\cdot\operatorname{curl}\mathbf{n})^2 + |\mathbf{n}\times\operatorname{curl}\mathbf{n}|^2 + \operatorname{tr}([\nabla\mathbf{n}]^2) = |\nabla\mathbf{n}|^2$$

to the energy expression (17), we obtain

$$\begin{aligned}\mathcal{E}[s, \mathbf{n}, \Omega] = {} & \frac{k_3}{2}\int_\Omega s^2\widetilde{\mathcal{W}}_1(\mathbf{n}, \nabla\mathbf{n})d\boldsymbol{x} \\ & + \gamma_0\int_\Omega w(s)\,d\boldsymbol{x} + \frac{1}{2}\int_\Omega b|\nabla s|^2 d\boldsymbol{x} \\ & + \frac{1}{2}a_0\left[\int_\Gamma s^2(\boldsymbol{v}\cdot\mathbf{n})^2 dS(\boldsymbol{x}) + \int_\Gamma (s - s_a)^2 dS(\boldsymbol{x})\right],\end{aligned}$$

where

$$\widetilde{\mathcal{W}}_1(\mathbf{n}, \nabla\mathbf{n}) = (k_1/k_3)(\operatorname{div}\mathbf{n})^2 + (k_2/k_3)(\mathbf{n}\cdot\operatorname{curl}\mathbf{n})^2 + |\mathbf{n}\times\operatorname{curl}\mathbf{n}|^2 + (k_2/k_3)\{\operatorname{tr}([\nabla\mathbf{n}]^2) - (\operatorname{div}\mathbf{n})^2\}. \tag{22}$$

C. Scaling and nondimensionalization

Introducing a length scale L_0 to be of the same order as R_c, and noting the scalings

$$\Omega = L_0^3\tilde{\Omega}, \quad \Gamma = L_0^2\tilde{\Gamma}, \quad \partial\Omega_0 = L_0^2\partial\tilde{\Omega}_0, \quad \nabla = \frac{1}{L_0}\tilde{\nabla},$$

where $\tilde{}$ denotes nondimensional quantities, (22) becomes

$$\begin{aligned}\mathcal{E}[s,\mathbf{n}] &= k_3L_0\tilde{\mathcal{E}}[s,\mathbf{n}]\\ \tilde{\mathcal{E}}[s,\mathbf{n}] &:= \frac{1}{2}\int_\Omega s^2\widetilde{\mathcal{W}}_1(\mathbf{n},\nabla\mathbf{n})\,d\boldsymbol{x}\\ &\quad + \frac{\tilde{b}}{2}\int_\Omega |\nabla s|^2 d\boldsymbol{x} + \tilde{\gamma}_0\int_\Omega w(s)d\boldsymbol{x}\\ &\quad + \frac{\tilde{a}_0}{2}\left[\int_\Gamma s^2(\boldsymbol{\nu}\cdot\mathbf{n})^2 dS(\boldsymbol{x}) + \int_\Gamma (s-s_a)^2 dS(\boldsymbol{x})\right],\end{aligned} \tag{23}$$

where

$$\tilde{b} = \frac{b}{k_3}, \quad \tilde{\gamma}_0 = \frac{L_0^2}{k_3}\gamma_0, \quad \tilde{k}_i = \frac{k_i}{k_3}, \quad i = 1,2, \quad \tilde{a}_0 = \frac{a_0L_0}{k_3}. \tag{24}$$

For convenience, we have dropped the $\tilde{}$ on all variables (the domains are now nondimensional). Since $w(s)$ is specified in Eqs. (4)–(6), the remaining parameters of the model reduce to the ratios in Eq. (24), which highlight the special role of the bending modulus k_3. Finally, let us recall that $\tilde{k}_1$ and $\tilde{k}_2$ penalize bending and twist, respectively, and $\tilde{\gamma}_0$ measures the energy of the disordered core and $\tilde{b}$ that of the interface (or transition layers) between the spooled and disorder regions of the capsid. The parameter $\tilde{a}_0$ penalizes the departure of the DNA arrangement from planar alignment on Γ. Our goal is to obtain minimizers of the energy (24) as

$$\lim \tilde{k}_i \to \infty, \quad i = 1,2, \quad \tilde{a}_0 \to \infty. \tag{25}$$

Since our approach is numerical, condition (25) will be reinterpreted accordingly [see statement (18)].

IV. PARAMETER ESTIMATES AND NUMERICAL SIMULATIONS

The evaluation of the bending constant K_3 in Eq. (2) will provide guidance to determine the remaining parameters in Eq. (24). As for semiflexible polymers and application to the DNA molecule, following Tzlil *et al.* [39,40], we take

$$K_3 = K_BTL_pm_0. \tag{26}$$

The DNA cross-sectional length density, m_0, is estimated by taking the ratio of the length of a DNA molecule to the volume of the container in which it is packed. Thus, for a perfectly packed DNA molecule (i.e., no empty space in the volume), the *maximum value* is $m_0 = 1/[\pi(d/2)^2] = 1.85131 \times 10^{17}\ \mathrm{m}^{-2}$, where we used an average, effective DNA diameter of $d = 2.6225$ nm from Table I. More realistically, for average bacteriophage genome (length 30.0624 μm) and capsid head (radius 34.11 nm), we get $m_0 = 1.809173 \times 10^{17}\ \mathrm{m}^{-2}$. Furthermore, taking a representative value of the persistence length $L_p = 54.49$ nm, our effective bending constant, at room temperature, is $k_3 = 4.058027 \times 10^{-11}$ J/m. Next, we choose the length scale $L_0 = R_c/0.4$, where 0.4 is the nondimensional radius of the computational capsid domain.

We observe that $k_3 = K_3(1+\alpha)$ [Eq. (20)] appears as a multiplicative constant in the energy, and its role is adjusting the pressure. We determine its order of magnitude with respect to K_3 by pressure measurements (see Sec. IV). This is an approach to determine model parameters proposed by Kléman and Lavrentovich [28] for chromonic liquid crystals.

Determining the parameters k_i, $i = 1, 2$, and $\tilde{a}_0$ satisfying the property (25) is an issue directly related to the discretization of the problem and so dependent on the step length size used in the numerical algorithm. In our calculations, we take

$$a_0 = 100 \quad \text{and} \quad k_1 = k_2 = 10k_3, \tag{27}$$

This yields $\tilde{a}_0 = 250$.

For the remaining parameters, we explore a broad range of values for $\tilde{b}$ and $\tilde{\gamma}_0$. Specifically, we take

$$0.1 \leqslant \tilde{b} \leqslant 5.0, \quad 0.1 \leqslant \tilde{\gamma}_0 \leqslant 20, \tag{28}$$

and compare the predicted core sizes with the available virus measurements shown in Table I.

The outcome from the numerical simulations is summarized in several figures. In Fig. 4, we see how the size of the inner disordered core is affected by $\tilde{b}$ and $\tilde{\gamma}_0$; increasing either parameter tends to shrink the radius of the disordered core. In addition, increasing $\tilde{b}$ also creates a steeper transition layer from well-ordered packing to disordered, i.e., changes from $s = 0.8$ to $s = 0$ happen over much shorter distances. Figure 5 shows how the internal "core radius" was estimated for a particular choice for $\tilde{b}$ and $\tilde{\gamma}_0$.

Figure 6 gives a 3D visualization of DNA packing via the director field $\mathbf{n}$ colored by the ordering parameter s. Recall that $\mathbf{n}$ only gives the (local) tangential orientation of the DNA strand but clearly $\mathbf{n}$ mimics spooling of DNA inside the capsid. Note that when s is close to zero (referring to the blue arrows in Fig. 6) the orientation of $\mathbf{n}$ is not well defined. In other words, our model does *not* say that spooling of the DNA is maintained up to the central axis of the capsid. The blue region should be interpreted as completely disordered.

Figure 7 shows how the capsid pressure and the core radius vary with $\tilde{b}$ and $\tilde{\gamma}_0$, which was generated by running simulations for several different values of $\tilde{b}$ and $\tilde{\gamma}_0$ and interpolating the simulation output data (namely, the pressure and core radius). Since we do not have access to detailed experimental visualizations of actual DNA packing, we chose $\alpha = 75$ to give a reasonable fit for the virus data in Table I. The constant core radius curves show how the same disordered core radius can be simulated for different choices of $\tilde{b}$ and $\tilde{\gamma}_0$. In principle, one can use the value of the pressure along the curve to fully determine the values of $\tilde{b}$ and $\tilde{\gamma}_0$ for a particular virus.

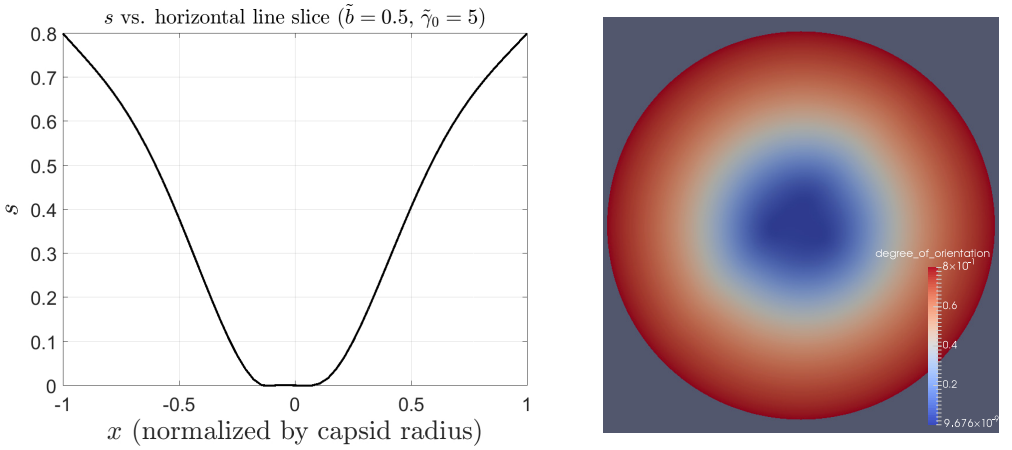

FIG. 5. The graphs show two different profiles of the order parameter in the capsid domain. Left plot is of s evaluated along a line through the equator of the capsid. The center of the capsid is located at 0, and the capsid radius is normalized to 1. Since the maximum order corresponds to $s = 0.8$, we take the disordered threshold at $s = 0.4$, which gives the ratio $r_0/R_c \approx 0.496$. Right plot: The order profile of the capsid transitioning from ordered DNA (red) to disordered (blue) as a 2D slice through the capsid equator.

However, it would be beneficial to have more data available to make this a more robust procedure.

V. SHAPE OPTIMIZATION

In this approach, the optimal energy of the packing configuration is the one that minimizes $\mathcal{E}$ in Eq. (23) with respect to s and $\mathbf{n}$. In order to compute pressures in the capsid at the minimum energy state, we perturb $\mathcal{E}$ with respect to the domain Ω, i.e., take shape derivatives of the energy [57]. This is a framework for "differentiating" a functional with respect to a "shape" variable. For example, these techniques can be used to find the shape of a wing such that its drag is minimized [58,59].

More specifically, given a (nondimensional) perturbation field $\mathbf{V}$ that deforms Ω, the shape variation $\delta_\Omega \tilde{\mathcal{E}}[s, \mathbf{n}, \Omega; \mathbf{V}]$ gives the (nondimensional) change in energy due to a change in the volume. For example, let $\mathbf{V}_\Gamma$ be a smooth vector field such that:

$$\mathbf{V}_\Gamma = \boldsymbol{\nu}, \text{ on } \Gamma, \text{ and smoothly decays to zero inside } \Omega. \quad (29)$$

Then the dimensional change in energy due to expanding the outer boundary Γ is $k_3 \delta_\Omega \tilde{\mathcal{E}}[s, \mathbf{n}, \Omega; \mathbf{V}_\Gamma]$ which has units, J/m, of force. Thus, the average (dimensional) pressure being exerted on the boundary of the capsid Γ is

$$\text{outer pressure} = \frac{1}{L_0^2 |\Gamma|} k_3 \delta_\Omega \tilde{\mathcal{E}}[s, \mathbf{n}, \Omega; \mathbf{V}_\Gamma], \quad (30)$$

where we note that $|\Gamma|$ is the nondimensional surface area of the capsid. Note that $\mathbf{V}_\Gamma$ is normalized so that $|\mathbf{V}_\Gamma| = 1$ on Γ. The particular form of the extension in Eq. (29) does not matter because ultimately the shape derivative only depends on what happens at the boundary Γ by the Hadamard-Zolésio

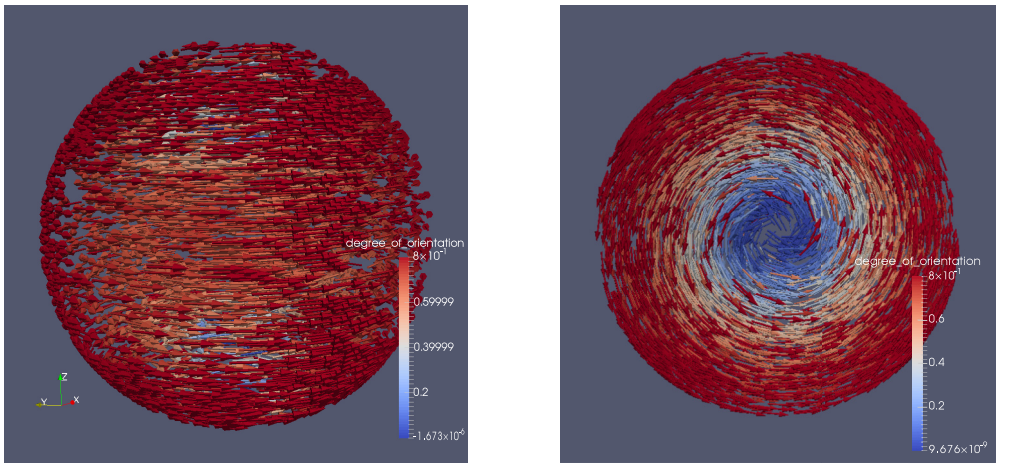

FIG. 6. Three-dimensional visualization of the director field $\mathbf{n}$ showing a spooling configuration. Left is a side view; right is a top view. The coloring of the arrows corresponds to the degree of orientation s, i.e., red indicates well ordering (spooling) of the DNA strand and blue is disordered.

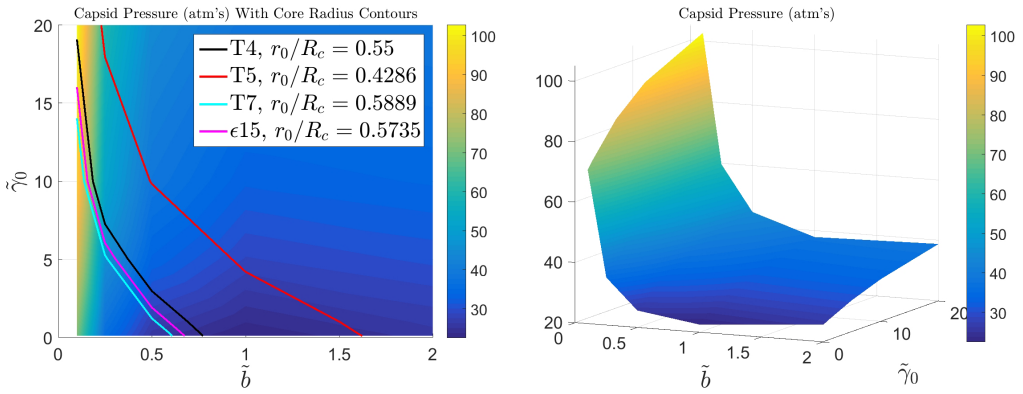

FIG. 7. Plots of core radius and capsid pressure. Left plot show curves of constant normalized core radius ($\frac{r_0}{R_c}$ for different choices of $\tilde{b}$ and $\tilde{\gamma}_0$ overlaid on the pressure values). In the region where the core radius matches experiment, the pressure values are also comparable to experimental values (from a minimum of about 26 atms to a maximum of about 95 atms). The right plot is a 3D view of the pressure. Note: α is chosen as 75, which fully determines k_3, to give a decent fit for all four viruses in Table I.

structure theorem [57]. The graphs of the pressure in terms of the parameters $\tilde{b}$ and $\tilde{\gamma}_0$ are shown in Fig. 7.

VI. CONCLUSIONS

We have constructed a model of encapsidation of viral DNA combining that of the hexagonal columnar liquid crystals with the theory of liquid crystals with variable degree of orientation. The model is accompanied by a finite-element-based algorithm for energy minimization, with design and prediction capabilities that may prove to be a real asset in applications. Due to the presence of the order parameter, the algorithm is able to deal with very general faceted capsid domains, including the geometry of the packing motor features, and also allows for the presence of knots in the DNA. The outcome of the model is a phase space for the radius of the disordered core and the pressure near the boundary of the capsid, with the potential to aid in the design of viral DNA to meet desired specifications. The model also allows for the exploration of parameter values, reiterating its value as a design tool.

Future extensions of this work will address the presence of ions and the dynamics of DNA ejection from the capsid. Furthermore, although axial symmetry is appropriate for the DNA packing problem, it is not strictly required by our model. Moreover, our continuum model can be combined with a direct model (e.g., molecular dynamics and Monte Carlo methods) as a way to reconstruct the global DNA molecule and study its topology. The benefits here would be faster simulation time, because the continuum model can provide a good initial configuration for the Monte Carlo simulation, and the details of the topological and geometrical entanglement of the DNA strand could then be explicitly determined.

ACKNOWLEDGMENTS

The authors are very grateful to the support granted to the project by the National Science Foundation through Grants No. NSF-DMS-1817156 (J.A. and M.V.), No. NSF-DMS-1816740 (M.C.C.), and No. NSF-DMS-1555222-CAREER (S.W.).

[1] H. S. Park and O. D. Lavrentovich, *Lyotropic Chromonic Liquid Crystals: Emerging Applications* (John Wiley & Sons, Hoboken, NJ, 2012).
[2] A. Leforestier and F. Livolant, Proc. Natl. Acad. Sci. USA **106**, 9157 (2009).
[3] A. Leforestier and F. Livolant, J. Mol. Biol. **396**, 384 (2010).
[4] J. Lepault, J. Dubochet, W. Baschong, and E. Kellenberger, EMBO J. **6**, 1507 (1987).
[5] D. Reith, P. Cifra, A. Stasiak, and P. Virnau, Nucleic Acids Res. **40**, 5129 (2012).
[6] R. L. Rill, Proc. Natl. Acad. Sci. USA **83**, 342 (1986).
[7] T. E. Strzelecka, M. W. Davidson, and R. L. Rill, Nature **331**, 457 (1988).
[8] H.-S. Park, S.-W. Kang, L. Tortora, Y. Nastishin, D. Finotello, S. Kumar, and O. D. Lavrentovich, J. Phys. Chem. B **112**, 16307 (2008).
[9] E. Kellenberger, E. Carlemalm, J. Sechaud, A. Ryter, and G. De Haller, Bacterial chromatin **1**, 11 (1986).
[10] F. Livolant, Physica A **176**, 117 (1991).
[11] A. Leforestier and F. Livolant, Biophys. J. **65**, 56 (1993).
[12] A. Leforestier, S. Brasiles, M. De Frutos, E. Raspaud, L. Letellier, P. Tavares, and F. Livolant, J. Mol. Biol. **384**, 730 (2008).
[13] D. Marenduzzo, E. Orlandini, A. Stasiak, L. Tubiana, C. Micheletti *et al.*, Proc. Natl. Acad. Sci. USA **106**, 22269 (2009).
[14] A. Fokine and M. G. Rossmann, Bacteriophage **4**, e28281 (2014).
[15] D. E. Smith, S. J. Tans, S. B. Smith, S. Grimes, D. L. Anderson, and C. Bustamante, Nature **413**, 748 (2001).
[16] I. J. Molineux and D. Panja, Nat. Rev. Microbiol. **11**, 194 (2013).

[17] A. Evilevitch, L. Lavelle, C. M. Knobler, E. Raspaud, and W. M. Gelbart, Proc. Natl. Acad. Sci. USA **100**, 9292 (2003).
[18] M. Jeembaeva, M. Castelnovo, F. Larsson, and A. Evilevitch, J. Mol. Biol. **381**, 310 (2008).
[19] S. C. Riemer and V. A. Bloomfield, Biopolymers **17**, 785 (1978).
[20] T. Liu, U. Sae-Ueng, D. Li, G. C. Lander, X. Zuo, B. Jönsson, D. Rau, I. Shefer, and A. Evilevitch, Proc. Natl. Acad. Sci. USA **111**, 14675 (2014).
[21] U. Sae-Ueng, D. Li, X. Zuo, J. B. Huffman, F. L. Homa, D. Rau, and A. Evilevitch, Nat. Chem. Biol. **10**, 861 (2014).
[22] M. R. Shaebani, J. Najafi, A. Farnudi, D. Bonn, and M. Habibi, Nat. Commun. **8**, 15568 (2017).
[23] J. Arsuaga, R. K.-Z. Tan, M. Vazquez, S. C. Harvey *et al.*, Biophys. Chem. **101**, 475 (2002).
[24] S. C. Harvey, A. S. Petrov, B. Devkota, and M. B. Boz, Phys. Chem. Chem. Phys. **11**, 10553 (2009).
[25] A. J. Spakowitz and Z.-G. Wang, Biophys. J. **88**, 3912 (2005).
[26] J. L. Ericksen, Arch. Rat. Mech. Anal. **113**, 97 (1991).
[27] P. G. de Gennes and J. Prost, *The Physics of Liquid Crystals* (Oxford University Press, Oxford, 1993).
[28] M. Kléman and O. D. Laverntovich, *Soft Matter Physics: An Introduction* (Springer, Berlin, 2002).
[29] E. F. Gramsbergen, L. Longa, and W. H. de Jeu, Phys. Rep. **135**, 195 (1986).
[30] W. C. Earnshaw and S. R. Casjens, Cell **21**, 319 (1980).
[31] G. Effantin, P. Boulanger, E. Neumann, L. Letellier, and J. Conway, J. Mol. Biol. **361**, 993 (2006).
[32] M. E. Cerritelli, N. Cheng, A. H. Rosenberg, C. E. McPherson, F. P. Booy, and A. C. Steven, Cell **91**, 271 (1997).
[33] K. Wissbrun, Faraday Discuss. Chem. Soc. **79**, 161 (1985).
[34] L. R. Comolli, A. J. Spakowitz, C. E. Siegerist, P. J. Jardine, S. Grimes, D. L. Anderson, C. Bustamante, and K. H. Downing, Virology **371**, 267 (2008).
[35] J. Chang, P. Weigele, J. King, W. Chiu, and W. Jiang, Structure **14**, 1073 (2006).
[36] W. Jiang, J. Chang, J. Jakana, P. Weigele, J. King, and W. Chiu, Nature **439**, 612 (2006).
[37] A. Cordova, M. Deserno, W. M. Gelbart, and A. Ben-Shaul, Biophys. J. **85**, 70 (2003).
[38] P. Grayson, A. Evilevitch, M. M. Inamdar, P. K. Purohit, W. M. Gelbart, C. M. Knobler, and R. Phillips, Virology **348**, 430 (2006).
[39] S. Tzlil, J. T. Kindt, W. M. Gelbart, and A. Ben-Shaul, Biophys. J. **84**, 1616 (2003).
[40] W. Klug and M. Ortiz, J. Mech. Phys. Solids **51**, 1815 (2003).
[41] P. Leiman, S. Kanamaru, V. Mesyanzhinov, F. Arisaka, and M. Rossmann, Cell. Mol. Life Sci. **60**, 2356 (2003).
[42] N. H. Olson, M. Gingery, F. A. Eiserling, and T. S. Baker, Virology **279**, 385 (2001).
[43] L. Ambrosio, Manuscr. Math. **68**, 215 (1990).
[44] R. H. Nochetto, S. W. Walker, and W. Zhang, SIAM J. Numer. Anal. **55**, 1357 (2017).
[45] R. H. Nochetto, S. W. Walker, and W. Zhang, J. Comput. Phys. **352**, 568 (2018).
[46] S. W. Walker (unpublished).
[47] L. Hiltner and M. Calderer, Ph.D. thesis, University of Minnesota, 2018.
[48] W. S. Klug, M. T. Feldmann, and M. Ortiz, Comput. Mech. **35**, 146 (2005).
[49] S. Walker, Felicity: Finite element implementation and computational interface tool for you, 2019, https://www.math.lsu.edu/~walker/software.html.
[50] F.-H. Lin, Comm. Pure Appl. Math. **44**, 453 (1991).
[51] E. G. Virga, *Variational Theories for Liquid Crystals* (Chapman & Hall, London, 1994).
[52] A. E. Diegel and S. W. Walker (unpublished).
[53] A. Morvant, E. Seal, and S. W. Walker (unpublished).
[54] F. H. Lin and C. C. Poon, J. Geom. Anal. **4**, 379 (1994).
[55] L. Ambrosio, Manuscr. Math. **68**, 309 (1990).
[56] R. Hardt, D. Kinderlehrer, and F.-H. Lin, Commun. Math. Phys. **105**, 547 (1986).
[57] S. W. Walker, *The Shapes of Things: A Practical Guide to Differential Geometry and the Shape Derivative*, 1st ed., Advances in Design and Control, Vol. 28 (SIAM, Philadelphia, PA, 2015).
[58] O. Pironneau, J. Fluid Mech. **64**, 97 (1974).
[59] R. Glowinski and O. Pironneau, J. Fluid Mech. **72**, 385 (1975).